Research Article

Jinhao Wang, Zhudan Li, and Baohong Jin*

Axial compression behavior and stress-strain relationship of slurry-wrapping treatment recycled aggregate concrete-filled steel tube short columns

https://doi.org/10.1515/rams-2023-0117 received February 13, 2023; accepted August 27, 2023

Abstract: The utilization of recycled concrete can effectively solve the problems of large accumulations of construction waste and the constant consumption of natural aggregates. Slurry-wrapping modification and concretefilled steel tubes (CFSTs) are effective approaches to enhance the utilization ratio of recycled concrete. The study involved 4 ordinary CFST columns and 16 slurry-wrapping recycled aggregate concrete-filled steel tube (SRACFST) columns. The variable parameters included the slurry-wrapping recycled aggregate replacement ratio and the section form. The result shows that the ultimate strength of the specimens reached the minimum and maximum at 25 and 100% aggregate replacement ratio. The favorable strength performance of the SRACFST columns is attributed to the dominant positive effect of the slurry-wrapping treatment in reducing matrix porosity over the negative impact of the recycled aggregate's complex interface transition zone. Due to the hoop factor, the residual bearing ratio peaks at a 25% substitution ratio. Four design standards were used to predict the ultimate strength, with GB50936 and EC4 yielding more accurate estimations, while AISC360-10 and AIJ provided conservative estimations. This study presents the equations of the stress-strain curve for the whole axial compression process, which can be directly applied in the theoretical and numerical analysis of RACFST columns.

Jinhao Wang: College of Civil and Hydraulic Engineering, Ningxia University, Yinchuan 750021, China

Zhudan Li: College of Civil and Hydraulic Engineering, Ningxia University, Yinchuan 750021, China; Zhongwei Emergency Management Bureau, Zhongwei 755000, China **Keywords:** recycled concrete-filled steel tube, stress–strain expression, slurry-wrapping aggregate treatment

1 Introduction

In the global construction industry, population growth has brought forth two significant challenges: the excessive consumption of non-renewable resources and the massive accumulation of construction waste [1]. Extensive stone quarrying has resulted in the depletion of aggregate resources and various ecological problems [2-4]. Consequently, an increasing number of nations are considering using recycled concrete to reduce their reliance on ordinary concrete. However, due to the high water absorption, large crushing index, low apparent density, and complex interface transition zone (ITZ) of recycled aggregate, the mechanical properties of recycled concrete are inferior to those of ordinary concrete [5,6]. From the perspective of mortar sticking to the recycled aggregate surface, two main methods for enhancing the physical properties of recycled concrete are considered: strengthening old mortar and removing old mortar [7]. Strengthening old mortar methods that do not introduce components other than recycled concrete has potent effects, such as carbonation treatment, nano-SiO2 treatment, and slurry-wrapping treatment [8–10].

The carbonation treatment shows an initial rapid enhancement rate, followed by a slower rate. Pre-soaking in $Ca(OH)_2$ solution prior to treatment significantly increases the carbonation rate, but it results in $Ca(OH)_2$ enrichment, which affects the quality of concrete [11,12]. The nano-SiO₂ treatment effectively enhances concrete strength. However, nanomaterials tend to agglomerate, leading to higher construction quality requirements [12]. Wang *et al.* [13] compared the slurry-wrapping treatment to the carbonation treatment. They concluded that the former not only reduces poor compatibility issues caused by high water absorption but also

^{*} Corresponding author: Baohong Jin, College of Civil and Hydraulic Engineering, Ningxia University, Yinchuan 750021, China, e-mail: jinbaohong@nxu.edu.cn

exhibits superior resistance to chloride ion penetration. Wang et al. [14] conducted an experiment on pre-soaking various recycled aggregates. The results indicated that, regarding the crushing index and strength improvement, the slurry-wrapping treatment with a 0.5 water/cement ratio outperformed the nano-SiO₂ treatment. Poon et al. [6] examined the ITZ between the aggregate and the matrix by preparing concrete with three distinct aggregates. This study confirmed that ITZ is a critical factor influencing recycled concrete strength. Martirena et al. [10] demonstrated that slurry-wrapping treatment could enhance the impermeability and porosity of recycled aggregate. Additionally, the treatment facilitated the formation of a thinner and denser ITZ within the concrete. Shi et al. [15] investigated the ITZ of recycled concrete, revealing that pozzolan slurry treatment increased the microhardness and density of the ITZ. The literature demonstrates that the slurry-wrapping treatment has advantages over other modifications, including resistance to chloride ion penetration, improved physical properties of aggregates, and enhanced ITZ. However, these modification methods in the literature have been applied to concrete rather than composite members.

Concrete-filled steel tube (CFST) columns are extensively used in multi-story buildings, bridges, offshore structures, and heavy industrial buildings due to their inherent advantages, including high ductility, strength, and seismic performance [16-18]. Tam et al. [19] proposed using recycled concrete to fill the steel tubes in order to incorporate environmental protection measures in CFST column preparation. Xiao et al. [20] performed an axial compression test on recycled aggregate concrete-filled steel tube (RACFST) specimens. The results indicated that the confinement of steel tubes significantly improved the strength and ultimate strain of the core recycled concrete. Ke et al. [21] conducted a high-temperature test of CFST columns. They observed that larger steel tube diameters resulted in more damage to the core concrete. Zhang et al. [22] found that the ultimate bearing capacity and ductility of square RACFST specimens decreased with an increasing replacement ratio. Lyu et al. [23] conducted axial compressive tests on RACFST specimens. The results revealed that the ultimate strength of square and circular RACFST specimens at 100% recycled aggregate replacement decreased by only 6.5 and 7.3%, respectively. Zhou et al. [24] conducted an axial compression test on 32 high titanium slag CFST columns. They found that the hoop coefficient significantly influenced the bearing capacity of short columns, but its effect on medium-long columns was not as pronounced. Bahrami and Nematzadeh [25] and Karimi et al. [26] conducted tests on CFST columns containing rock wool waste and tire rubber. The results showed that while specimens with these waste materials exhibited inferior mechanical properties compared to ordinary CFST, they displayed good

high-temperature resistance. Liang et al. [27,28] and Lin et al. [29] performed a series of axial compression tests and proposed the strength calculation models for CFRP-strengthened RACFST columns. The results indicated that specimens with a higher replacement ratio had lower axial stress but larger strain at the peak point [27]. The FRP-confined RACFT column with a higher replacement ratio exhibited a smaller axial strength but tended to exhibit more ductile behavior [28]. The proposed strength calculation models provided more accurate predictions [27-29]. de Azevedo et al. [30] suggested that the composite section exhibits a ductile response, and the ductility of ordinary CFST columns is higher than that of RACFST columns. These findings indicate that RACFST columns still possess a certain bearing capacity, despite their limitations relative to ordinary CFST columns. Additionally, their studies mainly focused on the effect of aggregate type, steel tube length, and fiber type on the RACFST column.

Utilization of construction waste is vital to environmental protection, carbon emission reduction, and ore resource conservation. The use of unmodified recycled aggregates in RACFST columns has limitations. It is worthwhile for scholars to study how to improve the utilization ratio of recycled aggregates while ensuring the quality of RACFST columns. Previous studies mainly focused on the effect of aggregate type on RACFST columns, and there were few studies on modified recycled aggregates on RACFST columns. Slurry-wrapping treatment can improve the quality of recycled concrete. Meanwhile, steel tube confinement can improve the performance of recycled concrete. However, few studies have combined the two methods to enhance recycled concrete strength.

Currently, there are limited studies reporting on RACFST columns filled with modified recycled aggregates. This study utilized the slurry-wrapping treatment and steel tubes to enhance the bearing capacity of recycled concrete. Twenty CFST columns were prepared, using the slurry-wrapping aggregate replacement ratio and the steel tube section form as the variation parameters. The axial compressive test revealed the failure mechanism and bearing capacity of the slurry-wrapping RACFST (SRACFST) columns. Moreover, the experiment offers valuable insights for the future application of recycled aggregates in CFST columns.

2 Test overview

2.1 Concrete material properties

Type I Portland cement 42.5 R and Type I fly ash were used for all specimen preparations. A polycarboxylate superplasticizer with a 20% water reduction was produced by

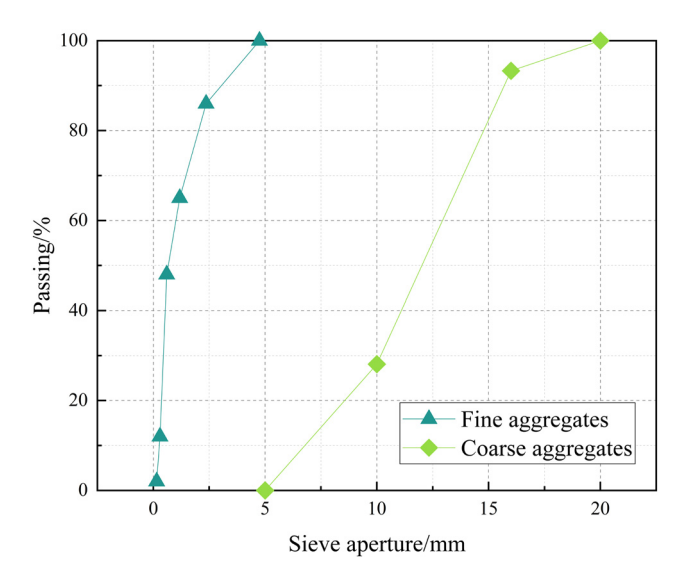


Figure 1: Particle size distribution curve.

Beijing Muhu Admixture Co., which was used to enhance concrete workability. Locally produced manufactured sand with a continuous gradation of 0–5 mm was used as fine aggregates. The recycled aggregate, obtained from disused C30 road pavement, was screened to a particle size of 5–20 mm after secondary crushing. Figure 1 illustrates the particle size distribution curve, tested according to JGJ 52-2006 [31].

2.2 Slurry-wrapping treatment process

To apply the cement slurry for the recycled coarse aggregate, three particle size ranges were used: 5–10, 10–16, and 16–20 mm. The slurry had a water/cement ratio of 0.5 and a fly ash content of 20%. The recycled coarse aggregates were soaked in the slurry, stirred thoroughly for 10 min, poured into a sieve, and rubbed until the slurry stopped dripping. Then, the aggregates were transferred indoors to a shaded area for curing for 3 days before being used in concrete. While transferring the aggregates to the shade, try to

separate them. The aggregates of 5–10 mm were found to be difficult to separate. Table 1 and Figure 2 display the basic physical properties and appearance of aggregates.

2.3 Steel material properties

The test coupons were made from the same batch of Q235 steel tubes, and testing was conducted following GB/T 228.1-2010 [32]. The stress–strain curve is presented in Figure 3. Table 2 shows Young's modulus (E_s), yield stress (f_y), corresponding strain at the yield stress (ε_y), ultimate stress (f_u), corresponding strain at the ultimate stress (ε_u), and Poisson's ratio (ν).

2.4 Specimen preparation

The 20 specimens were divided into two series: square sections (S series) and circular sections (C series). Five mix proportions were used, which varied with the replacement ratios (the mass percentages of natural aggregate replaced by slurry-wrapping recycled aggregate in concrete). The replacement ratios corresponded to 0 (natural aggregate) and 25, 50, 75, and 100% (slurry-wrapping recycled aggregate). All specimens had a wall thickness of 2 mm and a length of 400 mm. The square specimens had a side length of 100 mm, while the circular tubes had a diameter of 114 mm. Two identical specimens were prepared for each series and replacement ratio to minimize the accidental error. A uniform water/ cement ratio of 0.7:0.3:0.41:1.76:1.69 (cement: fly ash: water: sand: coarse aggregate) was used for all concretes. One tube end was welded with a 10 mm thick steel plate, and the concrete was poured in from the open end. After being cured in water for 28 days, the other end was finally welded with a steel plate of the same size. Three $100 \times 100 \times 100$ cubic blocks were prepared simultaneously and tested for compressive strength in accordance with GB/T 50081-2019 [33]. The

Table 1: Basic physical properties of aggregates

Туре	Particle size range (mm)	Water absorption (%)	Moisture content (%)	Crushing index (%)	Apparent density (kg·m ⁻³)	Bulk density (kg·m ⁻³)
Natural aggregate	5–20	0.74	0.37	8.8	2,708	1,496
Recycled aggregate	5–20	7.33	2.13	12.5	2,714	1,335
Slurry-wrapping recycled aggregate	5–20	5.70	2.19	12.3	2,723	1,378

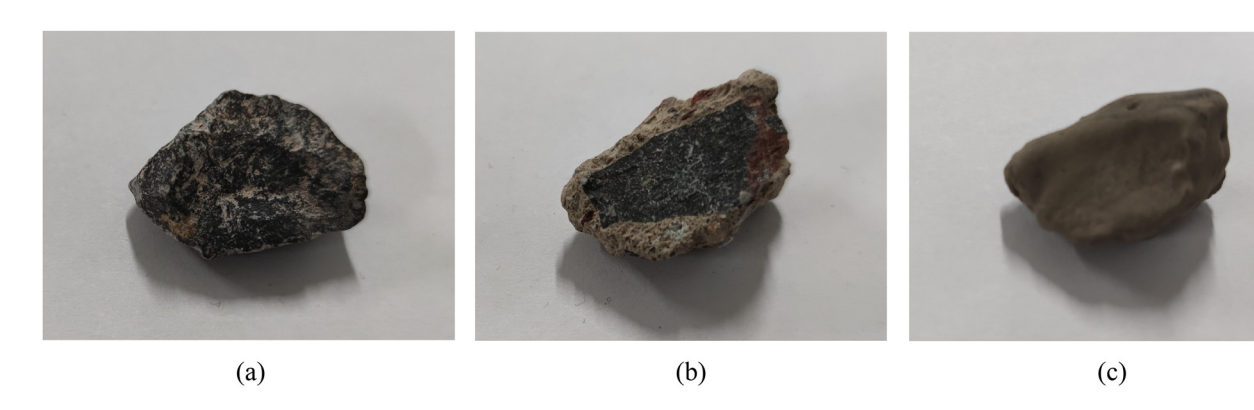


Figure 2: Appearance of three types of coarse aggregates: (a) natural aggregate, (b) recycled aggregate, and (c) slurry-wrapping recycled aggregate.

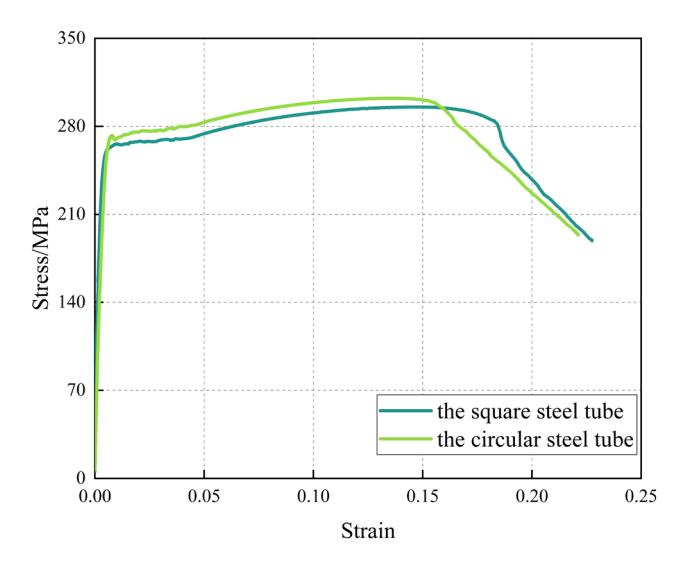


Figure 3: Tested stress-strain curves of steel.

substitution ratio (r), length (L), width (B) or diameter (D), thickness (t), yield strength (f_y), cube compressive strength (f_c), prism compressive strength (f_{ck}), hoop coefficient (θ), and ultimate strength (N_u) of the specimen are shown in Table 3.

2.5 Test loading system and measuring point arrangement

The test was conducted using a two-stage graded loading system [34]. In the first stage (0–0.6 $P_{\rm u}$, predicted ultimate

load capacity), the specimen was loaded at a rate of $P_{\rm u}/10$ per level. In the range of 0.6–0.9 $P_{\rm u}$, the specimen was loaded at a rate of $P_{\rm u}/15$ per level. The load was held constant for 2 min at each level. In the second stage, once the load reached 0.9 $P_{\rm u}$, the loading system switched to displacement control with a 1 mm·min⁻¹ loading rate. The loading was stopped when the specimen was seriously damaged [35].

The test setup is illustrated in Figure 4a. The loading equipment was the SHT-4106 pressure testing machine manufactured by Meters Industrial Systems (China) Co., Ltd. Four YHD-100 displacement gauges were positioned around the specimen. Four sets of strain gauges were symmetrically positioned in the middle of the specimen. Each set of strain gauges included a vertically arranged transverse strain gauge and a longitudinal strain gauge, as shown in Figure 4b.

3 Test results and analysis

3.1 Test phenomena and failure patterns

Figure 5a and b shows the failure pattern of all specimens. During the early loading stage, the surface of all specimens underwent minimal changes. When subjected to the ultimate strength, the middle and upper portions of square specimens and the circumference of circular specimens exhibited slight bulging. At the most unfavorable position

Table 2: Physical properties of steel

Туре	$E_{\rm s}$ (GPa) $f_{\rm y}$ (MPa)		$\varepsilon_{ m y}$ (mm·mm $^{-1}$)	f _u (MPa)	$\varepsilon_{\rm u}$ (mm·mm $^{-1}$)	N (mm·mm ⁻¹)	
Square steel tube	203.4	262.5	0.00598	295.4	0.14738	0.33	
Circular steel tube	202.2	272.5	0.00754	302.4	0.13422	0.33	

Table 3: Basic parameters and measured strength of specimens

Туре	R (%)	<i>L</i> (mm)	D(B) (mm)	t (mm)	f_{y} (MPa)	$f_{ m c}$ (MPa)	$f_{ m ck}$ (MPa)	θ	N _u (kN)
S-0-1/2	0	400	100	2	262.5	48.2	36.6	0.610	579.7
S-25-1/2	25	400	100	2	262.5	33.2	25.2	0.886	442.3
S-50-1/2	50	400	100	2	262.5	43.6	33.1	0.675	531.4
S-75-1/2	75	400	100	2	262.5	47.9	36.4	0.613	569.0
S-100-1/2	100	400	100	2	262.5	48.7	37.0	0.604	607.2
C-0-1/2	0	400	114	2	272.5	48.2	36.6	0.552	722.4
C-25-1/2	25	400	114	2	272.5	33.2	25.2	0.801	577.2
C-50-1/2	50	400	114	2	272.5	43.6	33.1	0.610	675.0
C-75-1/2	75	400	114	2	272.5	47.9	36.4	0.555	717.1
C-100-1/2	100	400	114	2	272.5	48.7	37.0	0.546	736.2

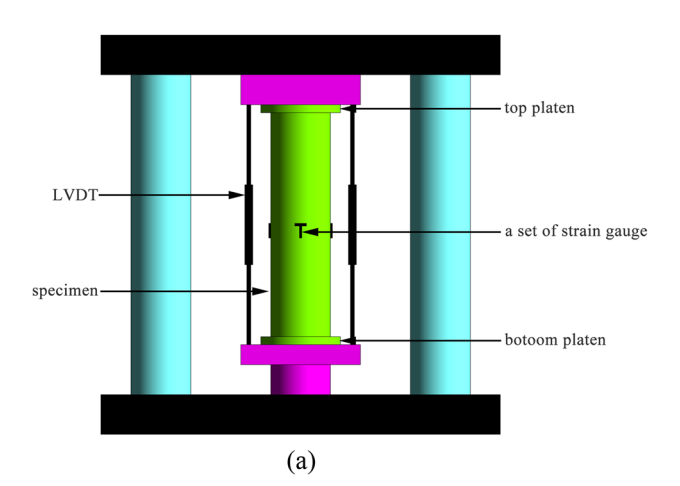
Note: $\theta = (f_v \times A_s)/(f_{ck} \times A_c)$; $A_s =$ section area of steel tube; $A_c =$ section area of concrete.

where the bulge occurred, the deformation of specimens increased sharply with displacement. At the end of the test, the square specimens exhibited cracks at the weld, and one or two prominent bulging rings appeared in the middle and upper parts. This occurred because the coarse aggregate sank due to gravity when the concrete was being prepared. As a result, the lower part of the specimen became denser, leading to higher bearing capacity and no appearance of bulging rings [22]. Figure 5c illustrates that the square specimens exhibited the typical waist-bulge damage pattern. Figure 5d shows that the circular specimens had one to two obvious bulges along a certain diagonal direction, which represented the typical shear sliding failure. After dismantling all the specimens, it was observed that regardless of the aggregate substitution ratio, the core concrete of square specimens was crushed at the bulge ring, while the circular specimens had an obvious diagonal shear crack at the bulge. Therefore, it can be concluded that the influence of section form on failure pattern is greater than that of the

replacement ratio [23,36,37]. The damage pattern of the specimens did not differ significantly with the substitution ratio, consistent with the previous study [38].

3.2 Load-displacement curves

Figure 6 shows the load—displacement curves of the square and circular specimens. The curves of the square specimens are sharper near the peak load, while those of the circular specimens are more rounded. The general trend of the square specimens remains relatively stable regardless of the aggregate substitution ratio. In the initial loading stage, the curves of the square specimens show a specific linear relationship, and they decrease rapidly after reaching the peak load, with the bearing capacity remaining basically unchanged. Different aggregate replacement ratios have an influence on the curve of circular specimens. At the beginning of loading, the curves of circular specimens have a



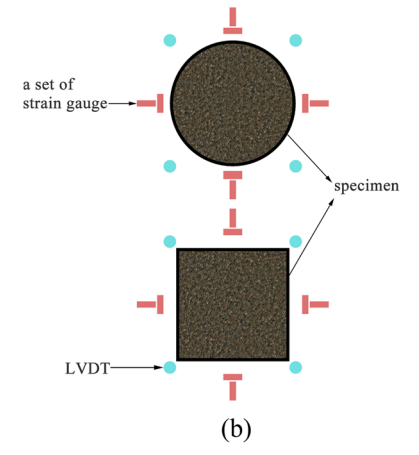


Figure 4: (a) Test setup and (b) measurement point arrangement.

6 — Jinhao Wang et al. DE GRUYTER



Figure 5: Failure patterns of specimens: (a) all the square specimens, (b) all the circular specimens, (c) square specimen destruction mode, (d) circular specimen destruction mode.

somewhat linear relationship. However, after reaching the peak load, the circular specimen curves drop relatively slowly, and the loads remain stable.

Figure 7 depicts the relationship between the specimens' ultimate strength $N_{\rm u}$ and ultimate displacement $\Delta_{\rm u}$ with different replacement ratios. The ultimate strength tends to first decrease and then increase as the replacement ratio increases, regardless of the section form. Figure 7a shows that under a 25% replacement ratio, the ultimate strength of specimens decreases the most, with the square and circular specimens decreasing by 23.7 and 20.1%,

respectively. At a low substitution ratio, the strength decreases due to the weakness of recycled aggregates [39]. However, when the replacement ratio increases to 100%, the ultimate strength increases the most, with the square specimens and circular specimens increasing by 4.7 and 1.9%, respectively. The strength of low- and medium-strength concrete is jointly determined by the ITZ and the porosity of the matrix [40]. Therefore, the strength decrease is attributed to the weakening of the ITZ by the recycled aggregates, resulting in a decrease in concrete strength. In addition, the strength increase is caused by the increase in under-hydrated active material on

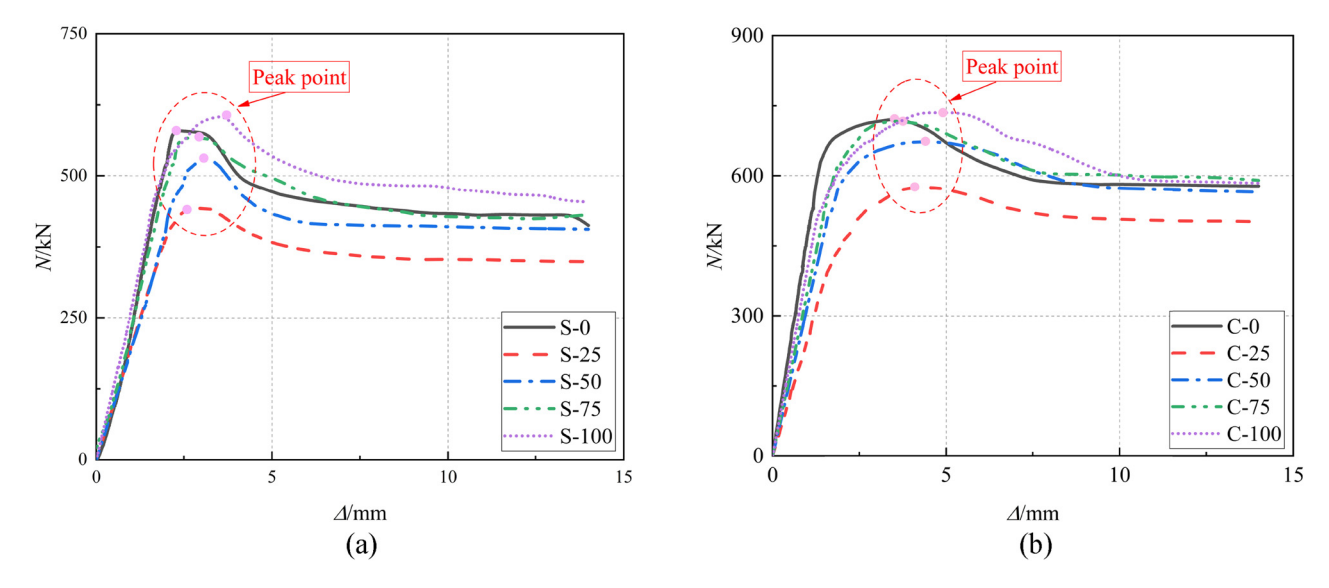


Figure 6: Load-displacement curves of specimens: (a) the square specimens, (b) the circular specimens.

the aggregate surface [41] and higher water absorption [42], which decreases the actual water/cement ratio and porosity of the matrix. The reduction in matrix porosity has a positive effect that outweighs the negative effect of ITZ weakening, resulting in an increase in concrete strength.

Figure 7b shows that the ultimate displacement of both square and circular specimens increases with the substitution ratios. Chen *et al.* [43] attributed the increase in ultimate displacement to the lower stiffness of recycled coarse aggregate compared to natural coarse aggregate. Figure 7b demonstrates a general increase in ultimate displacement with the replacement ratio, which may be attributed to the

decrease in recycled concrete's modulus of elasticity as the aggregate replacement ratio increases [44,45]. At a substitution ratio of 100%, the ultimate displacement of square specimens exhibits the highest increase, reaching 62.4%. Figure 7a and b and Table 3 indicate that, despite the hoop coefficient of square specimens being greater than that of circular specimens, the ultimate strength and ultimate displacement of circular specimens surpass those of square specimens, regardless of the replacement ratio. It suggests that circular specimens are more effective in restraining the core concrete than square specimens, which aligns with the previous study [36].

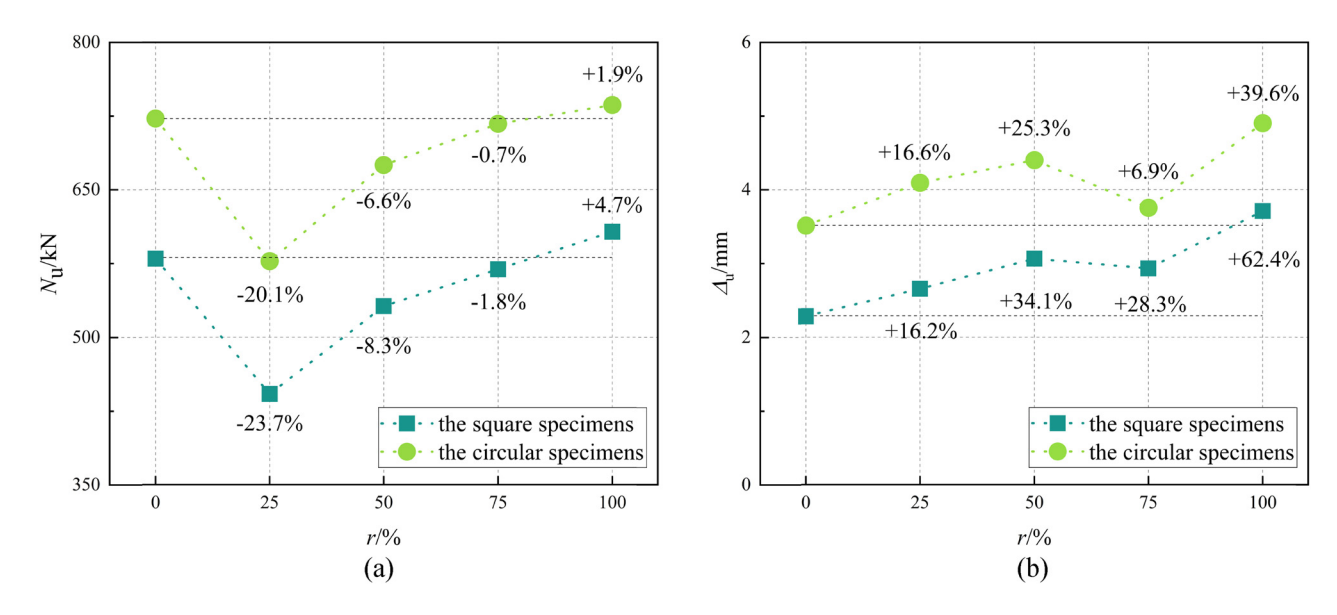


Figure 7: Performance comparison of specimens with replacement ratio: (a) ultimate strength, (b) ultimate displacement.

3.3 Load-strain curve

Figure 8 displays the load—strain curves of both square and circular specimens. During the initial loading stage, both square and circular specimens exhibit linear performance, with the slope of the axial strain greater than the lateral strain. The different Poisson's ratios between the steel tube and the core concrete result in each being under individual stress during this time, with the steel tube having a minimal impact on the concrete.

Following the end of the linear elastic stage, the square and circular specimens exhibit a distinct behavior with increasing load. In the case of most square specimens, the axial and transverse strains maintain a linear relationship until the load reaches $0.9\ N_{\rm u}$. Subsequently, the transverse strain increases at a faster rate, and the curve's slope begins to decrease. This occurrence can be attributed to the lateral expansion of the core concrete, resulting in the emergence of a bonding force with the steel tube. When the load reaches $0.75\ N_{\rm u}$, the axial and transverse strains of circular specimens experience a sudden increase. This sudden increase can be attributed to the decrease in bonding force, indicating that the specimen has entered the yield state.

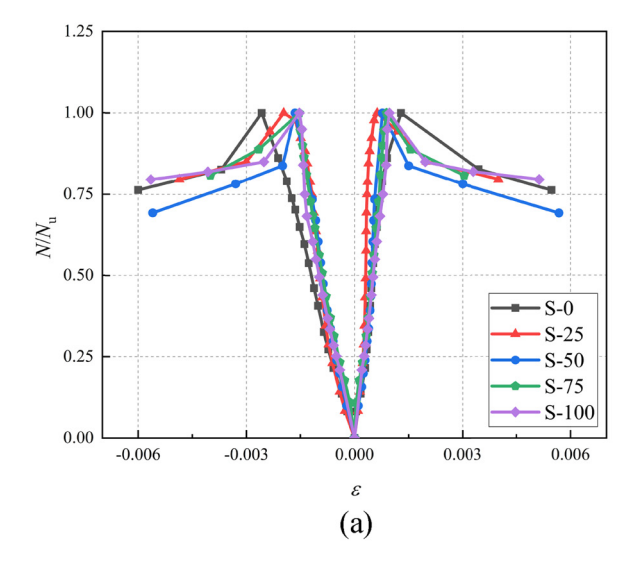
Upon reaching $N_{\rm u}$, the curves vary based on the section form of the specimen. In Figure 8a, it can be observed that the load of square specimens decreases sharply with a small strain and then stabilizes, resulting in a prominent point in the load–strain curve. In contrast, the strain increases sharply for circular specimens as shown in Figure 8b, but the load decreases to a lesser extent, resulting in a relatively smoother load–strain curve. This observation suggests that

circular specimens have better deformation capacity than square specimens. The difference in deformation capacity is attributed to the more uniform distribution of contact pressure between the tube wall and the core concrete in circular specimens [46]. Rectangular sections experience stress concentrations at the corners, while the constraint near the flat edge is insufficient [47].

Figure 8 shows that the different replacement ratios have a minimal impact on the load–strain curves in the early stage. However, after the specimens have yielded, the curves for different replacement ratios begin to diverge. The influence of the replacement ratios on the ultimate strain is irregular. The replacement ratios have a certain influence on the subsequent load–strain curve, but no significant regular pattern is observed.

3.4 Lateral deformation factor

The lateral deformation factor μ is the ratio of the transverse strain to the longitudinal strain. Figure 9 displays the lateral deformation factor of the specimens. It can be observed that the substitution ratio has a minimal effect on the curves, while the cross-section form significantly influences the results. Circular specimens exhibit more regular curves compared to square specimens. The lateral deformation factor μ of circular specimens remains near 0.3 (Poisson's ratio of steel [35]) until the load reaches 0.8 $N_{\rm u}$. In contrast, Poisson's ratio for concrete is only 0.2 [23], which indicates the effective restraint effect of the circular section.



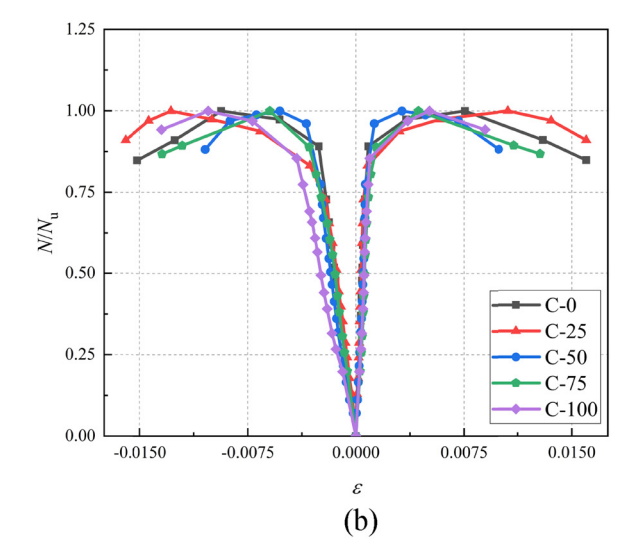


Figure 8: Load-strain curves of specimens: (a) the square specimens, (b) the circular specimens.

3.5 Analysis of test results

3.5.1 Initial stiffness K_0

The initial stiffness K_0 is a measure of a specimen's ability to resist elastic deformation under initial stress [48]. The calculation formula is defined as follows:

$$K_0 = \frac{N_{45\%}}{\Delta_{45\%}},\tag{1}$$

where $N_{45\%}$ is the strength of the specimens when the applied load reaches 45% of the ultimate strength before damage and $\Delta_{45\%}$ is the axial displacement of the specimens when the applied load reaches 45% of the ultimate load before damage.

Figure 10a illustrates that as the replacement ratios increase, the initial stiffness first decreases and then increases. This variation in initial stiffness is attributed to the impact of different replacement ratios on the compressive strength of the core concrete [49].

3.5.2 Residual bearing ratio α_r

The residual bearing ratio α_r is defined as the ratio of the minimum bearing capacity N_r to the ultimate strength N_u , which is used to measure the continuous bearing capacity of specimens after damage [50]. It is defined as follows:

$$\alpha_{\rm r} = \frac{N_{\rm r}}{N_{\rm u}}.$$
 (2)

Figure 10b illustrates that the residual bearing ratio exhibits an upward and then downward trend with the replacement ratio. The maximum residual bearing ratio occurs when the replacement ratio is 25%. This is due to the positive correlation between the residual bearing ratio and the hoop coefficient [51]. Once the hoop factor exceeds a specific value (about 4.5 and 1 for square and circular CFST specimens, respectively), the residual bearing capacity increases even after reaching the ultimate strength [23,52,53]. After reaching the ultimate strength, a higher residual bearing ratio is observed in specimens with lower core concrete strength, indicating a stronger restraint provided by the steel tubes.

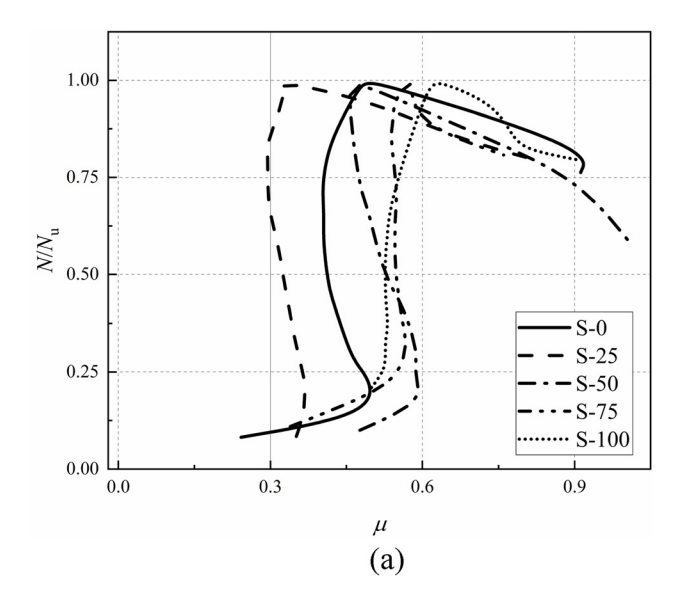
3.5.3 Strength improvement factor SI

The strength improvement factor SI, defined by Eqs. (3) and (4), represents the ratio of the ultimate strength $N_{\rm u}$ to the nominal strength $N_{\rm 0}$. It is used to measure the degree of strength improvement due to the interaction between the steel tube and the concrete.

$$SI = \frac{N_{\rm u}}{N_0},\tag{3}$$

$$N_0 = A_{\rm s} f_{\rm y} + A_{\rm c} f_{\rm c}'. {4}$$

Figure 10c illustrates that the strength improvement factor of all specimens is greater than 1, irrespective of the replacement ratio. It is attributed to the restraining effect of the steel tube [54], resulting in an ultimate



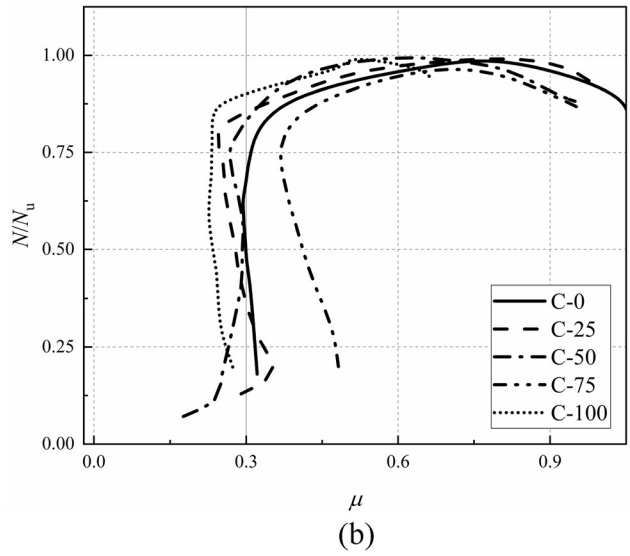


Figure 9: Lateral deformation factor of the specimens: (a) the square specimens, (b) the circular specimens.

10 — Jinhao Wang et al. DE GRUYTER

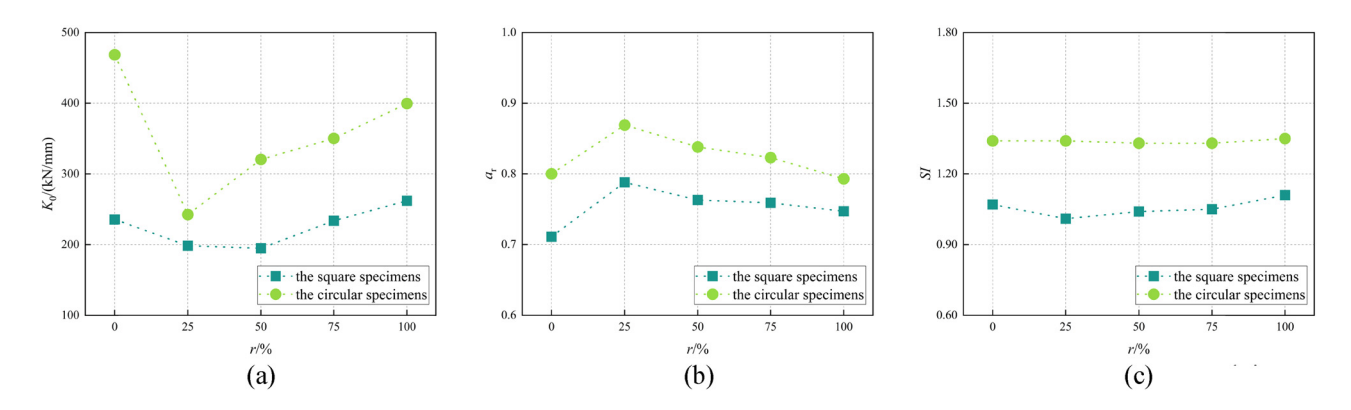


Figure 10: Analysis of test parameters: (a) initial stiffness, (b) residual bearing ratio, (c) strength improvement factor.

strength of the specimen that is significantly higher than the sum of the steel tube and concrete $(N_u/(A_sf_y + A_of_c') > 1)$. The strength improvement factor is greater for circular specimens than for square specimens. However, the change in strength improvement factor is insignificant for both square and circular specimens with the replacement ratio. It is likely due to the large diameter-to-thickness ratio, which leads to less confining pressure provided by the steel tube and less constraint on the internal core concrete [51].

4 Comparison of test values with national codes

The bearing capacity of CFST short columns with slurry-wrapping recycled aggregates was studied, and the test results were compared with the following codes: Chinese code GB50936 [55], European code EC4 [56], American code AISC360-10 [57], and Japanese code AIJ [58]. The tested compressive strength was transformed due to the different concrete shapes used for calculations in the various codes (prism in China, cylinder in Europe, USA, and Japan) [51]. The cylinder compressive strength ($f_{\rm cc}$) was obtained by converting the cubic compressive strength ($f_{\rm c}$) according to the European code (BS EN 1992-1-1-2004) [59]. The prism compressive strength ($f_{\rm ck}$) was obtained by converting the cubic compressive strength ($f_{\rm ck}$) according to the Chinese code (GB50010-2010) [60]. The conversion results are shown in Table 4.

4.1 Chinese code GB50936

Chinese code GB50936 treats the steel tube and the core concrete as a single entity, studying their combined compressive capacity, which is calculated by multiplying the combined

area of CFST (I_{sc}) and the compressive strength of CFST (I_{sc}). The conversion factors for the compressive strength of CFST (I_{sc}) and prism compressive strength (I_{ck}) depend on the section form. The calculation formulas are shown in the following:

$$N_{\rm CN} = A_{\rm sc} f_{\rm sc},\tag{5}$$

$$f_{\rm sc} = (1.212 + B\theta + C\theta^2) f_{\rm ck},$$
 (6)

where for the square specimens: $B = 0.131 f_y/213 + 0.723$, $C = -0.07 f_{ck}/14.4 + 0.026$; for the circular specimens: $B = 0.176 f_y/213 + 0.974$, $C = -0.104 f_{ck}/14.4 + 0.031$.

4.2 European code EC4

The European code EC4 calculates the CFST bearing capacity using the superposition method, where the total capacity is the sum of the bearing capacity of steel tubes and core concrete. It involves the sum of the products of steel tube area $A_{\rm s}$ and yield strength $f_{\rm y}$, and concrete area $A_{\rm c}$ and concrete compressive cylinder strength $f_{\rm cc}$, as shown in Eq. (7). When the section form is circular, and the relative slenderness ratio and eccentricity are small, the coefficients $\eta_{\rm s}$ and $\eta_{\rm c}$ can be used to reflect the increase in core concrete strength caused by constraint, as shown in the following equations:

Table 4: Conversion table of concrete compressive strength

Туре	NCA/ (MPa)	RCA ₁ / (MPa)	RCA ₂ / (MPa)	RCA ₃ / (MPa)	RCA ₄ / (MPa)
f_{c}	48.2	33.2	43.6	47.9	48.7
f_{cc}	36.6	25.2	33.1	36.4	37.0
f_{ck}	38.2	27.3	34.1	37.9	38.7

Note: f_c = the cubic compressive strength; f_{cc} = the cylindrical compressive strength; f_{ck} = the prismatic compressive strength.

$$N_{\rm EU} = A_{\rm s} f_{\rm v} + A_{\rm c} f_{\rm cc}, \tag{7}$$

$$N_{\rm EU} = \eta_{\rm s} A_{\rm s} f_{\rm y} + A_{\rm c} f_{\rm cc} \left[1 + \eta_{\rm c} \frac{t}{D} \frac{f_{\rm y}}{f_{\rm cc}} \right],$$
 (8)

$$\eta_{\rm s} = 0.25(3 + 2\overline{\lambda}) \le 1,\tag{9}$$

$$\eta_c = 4.9 - 18.5\overline{\lambda} + 17\overline{\lambda}^2 \ge 0,$$
(10)

where $\overline{\lambda}$ and the effective length coefficients are calculated according to the literature [51].

4.3 American code AISC360-10

The American code AISC360-10 uses the superposition method to calculate the strength. For the steel tube part, no correction factor is applied, while the concrete part uses correction factors of 0.85 and 0.95 for square and circular specimens, respectively, as shown in Eqs. (11) and (12).

$$N_{\rm US} = 0.658^{(f_{\rm y}A_{\rm s}+0.85A_{\rm c}f_{\rm cc})/P_{\rm e}}(f_{\rm y}A_{\rm s}+0.85A_{\rm c}f_{\rm cc}), \qquad (11)$$

$$N_{\rm US} = 0.658^{(f_y A_s + 0.95 A_c f_{cc})/P_e} (f_y A_s + 0.95 A_c f_{cc}), \qquad (12)$$

where $P_{\rm e}$ is calculated according to AISC360-10 [57] and the effective length factor is taken as 1.0.

4.4 Japanese code AIJ

The Japanese code AIJ uses the superposition method to calculate the strength. It applies different correction factors

to the calculation formulas for different section forms. For square sections, a correction factor of 0.85 is applied to the concrete part; while for circular sections, a correction factor of 1.27 is applied to the steel tube part. The calculation formulas for square and circular specimens are shown in the following equations, respectively:

$$N_{\rm JP} = A_{\rm s} f_{\rm v} + 0.85 A_{\rm c} f_{\rm cc},$$
 (13)

$$N_{\rm IP} = 1.27 A_{\rm s} f_{\rm v} + A_{\rm c} f_{\rm cc}.$$
 (14)

4.5 Comparative results

The calculation results are presented in Table 5 and Figure 11. It can be observed that the results of the GB50936 and EC4 codes are more accurate, both falling within ±9% of the error range. The EC4 code is the most accurate, with results ranging from –3 to +8%, but the GB50936 calculation is more stable. However, the AISC360-10 and AIJ codes are more conservative, with the maximum exceeding 36 and 20% of the measured values, respectively.

5 Axial compressive stress-strain analysis of the specimens

During the axial compression of the specimens, the deformation of the test points was too large and exceeded the permissible range of the strain gauges. The nominal

Table 5: Comparison of measured and calculated bearing capacity

Туре	Calculated values/(kN)			Measured value/(kN)	$N_{\rm u}/N_{\rm CN}$	$N_{\rm u}/N_{\rm EU}$	$N_{\rm u}/N_{\rm US}$	$N_{\rm u}/N_{\rm JP}$	
	N _{CN}	N _{EU}	N _{US}	N _{JP}	N _u				
S-0	620.4	557.9	499.4	505.0	579.7	0.93	1.04	1.16	1.15
S-25	483.8	457.4	415.6	419.7	442.3	0.91	0.97	1.06	1.05
S-50	578.4	520.1	467.9	472.9	531.4	0.92	1.02	1.14	1.12
S-75	617.9	555.1	497.1	502.7	569.0	0.92	1.03	1.14	1.13
S-100	625.3	562.5	503.2	509.0	607.2	0.97	1.08	1.21	1.19
Mean value						0.93	1.03	1.14	1.13
Standard deviation						0.05	0.08	0.10	0.10
Coefficients of variation						0.05	0.08	0.09	0.09
C-0	673.5	690.9	535.4	606.7	722.4	1.07	1.05	1.35	1.19
C-25	533.9	591.4	437.4	503.1	577.2	1.08	0.98	1.32	1.15
C-50	630.5	653.4	498.5	567.7	675.0	1.07	1.03	1.35	1.19
C-75	671.0	688.1	532.7	603.8	717.1	1.07	1.04	1.35	1.19
C-100	678.4	695.5	539.8	611.4	736.2	1.09	1.06	1.36	1.20
Mean value						1.08	1.03	1.35	1.18
Standard deviation						0.02	0.06	0.03	0.04
Coefficients of variation						0.02	0.06	0.02	0.03

12 — Jinhao Wang et al. DE GRUYTER

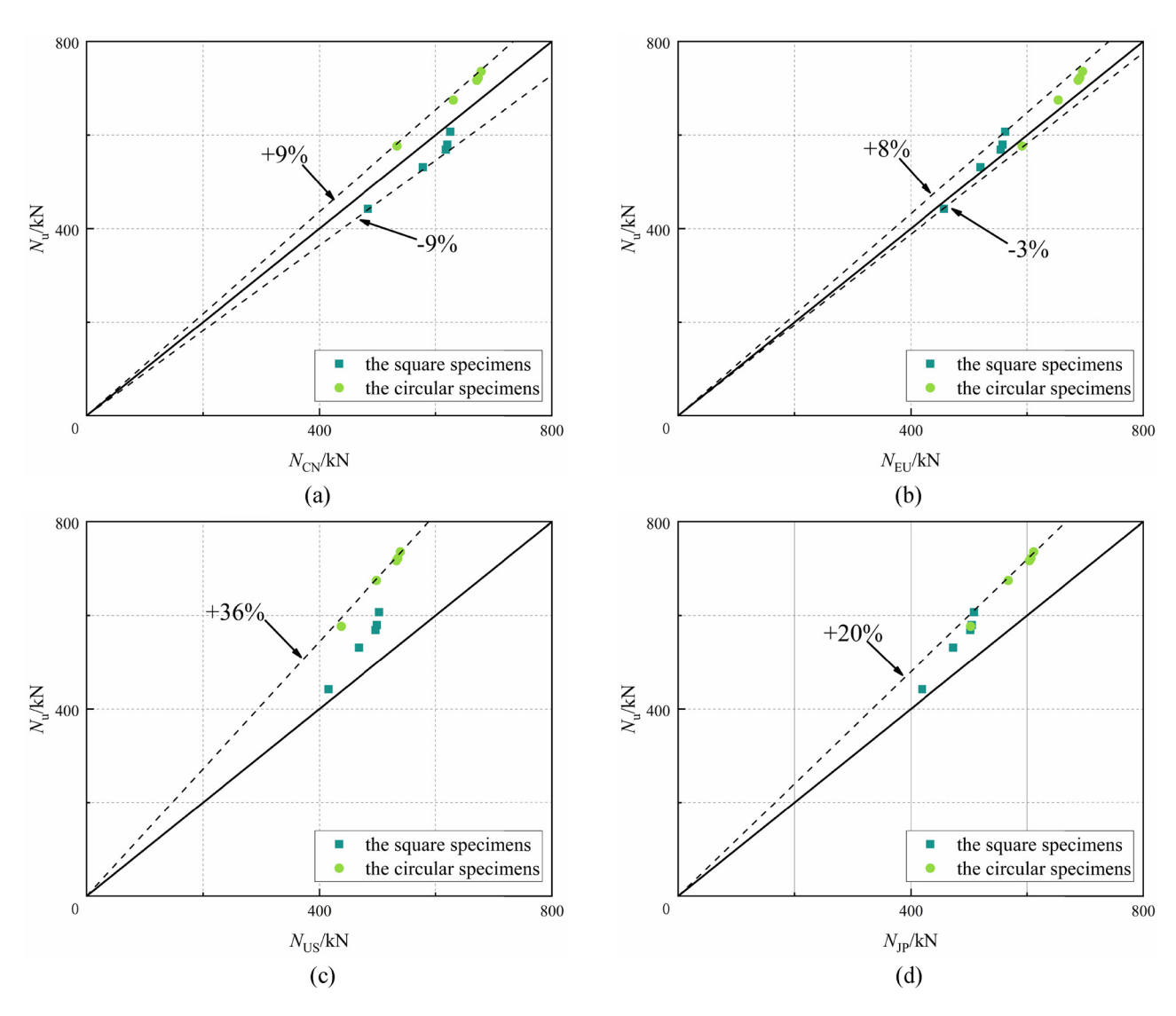


Figure 11: Comparison of experimental and calculated values: (a) GB50936, (b) EC4, (c) AISC360-10, (d) AIJ.

stress-strain curve of the specimens was obtained by transforming the measured axial displacement from the displacement gauges using the appropriate formula and normalizing it [61], as shown in Figure 12. Based on the observed trends, the curves in Figure 12a are divided into ascending, descending, and stable segments, while the curves in Figure 12b are divided into elastic, elastoplastic, descending, and stable segments. Mathematical models for square and circular specimens were established based on the test data from this study and the relevant literature [22,36,61], represented by Eqs. (15) and (16), respectively.

$$\begin{cases} Y = (A - 2)X^3 + (3 - 2A)X^2 + AX & (x \le 1) \\ Y = X^3/[X^3 + B(X - 1)^3 + (X - 1)^2] & (1 < x \le x_A), \\ Y = CX + D & (x > x_A) \end{cases}$$
 (15)

$$\begin{cases} Y = aX & (x \le x_a) \\ Y = b(X - 1)^2 + 1 & (x_a < x \le 1) \\ Y = cX^3 + dX^2 + eX + f & (1 < x \le x_b)' \\ Y = g & (x > x_b) \end{cases}$$
 (16)

where $X = \varepsilon/\varepsilon_{\rm u}$, $Y = \sigma/\sigma_{\rm u}$, $\varepsilon_{\rm u} = \varepsilon_{\rm scy}$, $\sigma_{\rm u} = f_{\rm scy}$, $f_{\rm scy}$ represents the calculated strength index of specimens, and $\varepsilon_{\rm scy}$ represents the strain corresponding to the specimen strength index $f_{\rm scy}$. For the square specimens, A is the parameter of the ascending section and is recommended to be set to 0.98; B and $x_{\rm A}$ are the parameters of the descending section, and their recommended values are 0.41 and 2.6, respectively; C and D are the stable section parameters, with recommended values of -0.01441 and 0.84289, respectively. For the circular specimen, a and a are the elastic section parameters and are suggested to take the values of

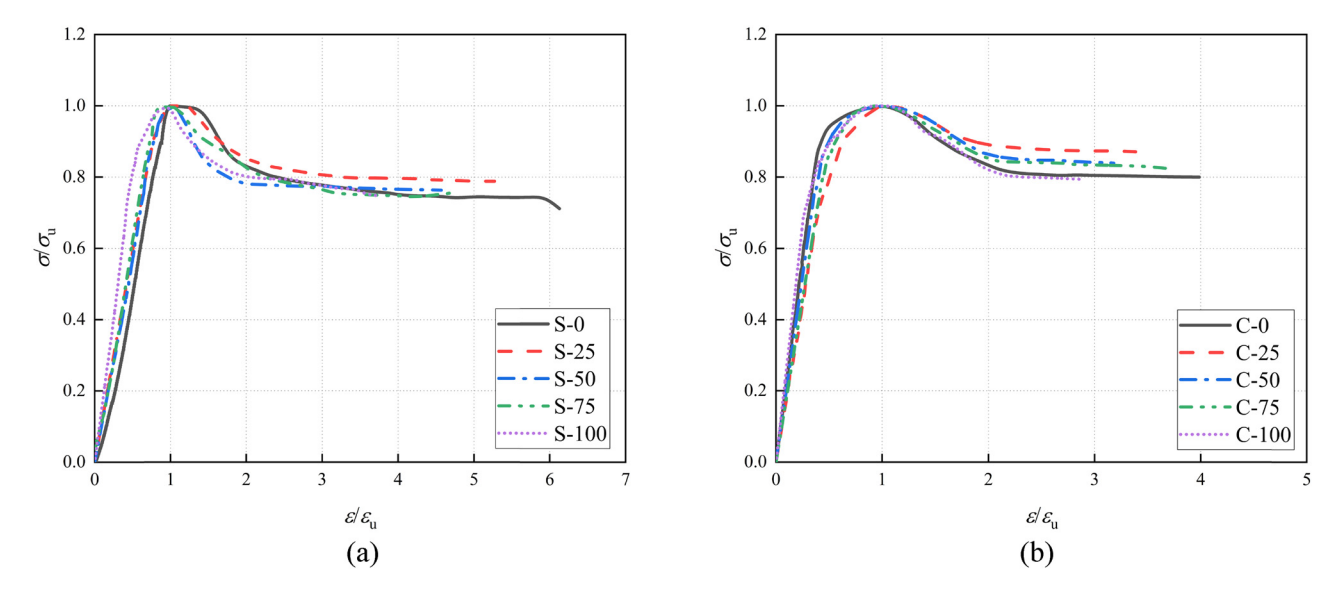


Figure 12: Dimensionless nominal stress-strain curves: (a) the square specimens, (b) the circular specimens.

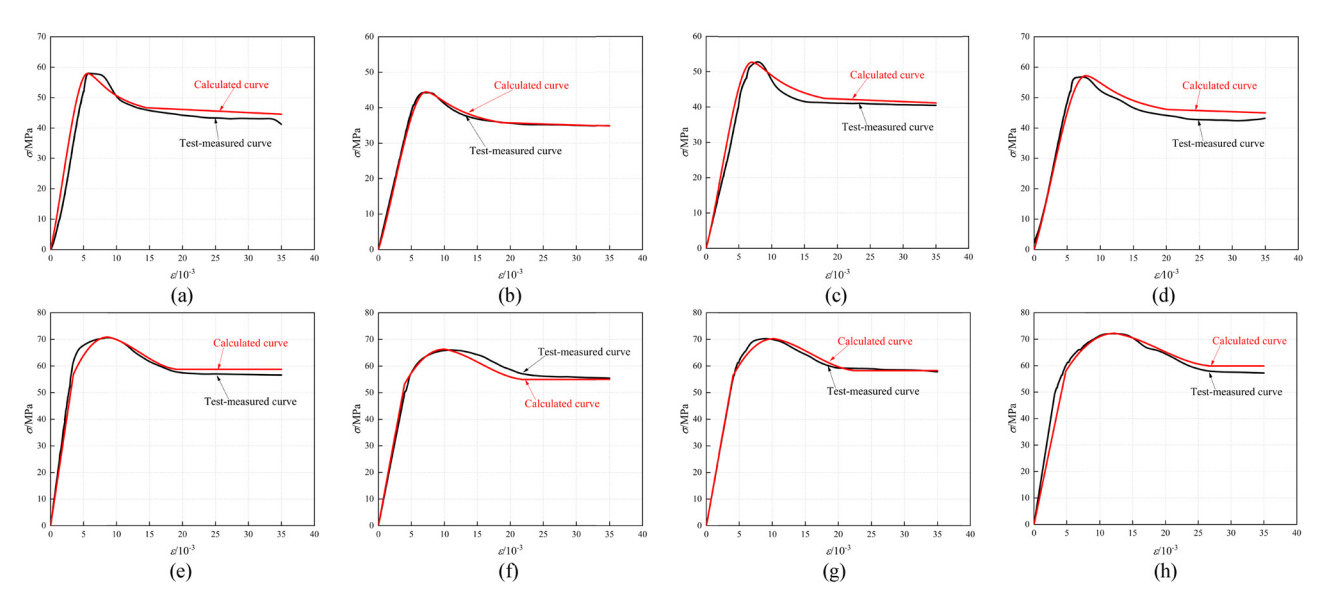


Figure 13: Comparison of calculated and test-measured stress-strain curves for part specimens: (a) S-0, (b) S-25, (c) S-50, (d) S-75, (e) C-0, (f) C-50, (g) C-75, (h) C-100.

2 and 0.4, respectively; b is the elastoplastic stage parameter and is recommended to be -0.55; c, d, e, f, x_b are the elastic section parameters, with recommended values of 0.1328, -0.6312, 0.81, 0.69, and 2.2, respectively; g is the parameter of the stable segment and is suggested to be set to 0.83.

This study analyzes the fundamental parameters that affect the working mechanism and mechanical properties of specimens. The influence of the slurry-wrapping recycled aggregate replacement ratio and cross-sectional forms on the ultimate stress and ultimate strain is taken into account. The GB50936 code, chosen for its accuracy and stability, is

used to establish stress-strain curve expressions for the whole process of the SRACFST specimens. The stress-strain curves for square and circular specimens are given in the following, respectively:

$$\sigma = f_{\text{scy}}(-1.02\varepsilon^{3} + 1.04\varepsilon^{2}\varepsilon_{\text{scy}} + 0.98\varepsilon\varepsilon_{\text{scy}}^{2})/\varepsilon_{\text{scy}}^{3}$$

$$(\varepsilon \leq \varepsilon_{\text{scy}})$$

$$\sigma = f_{\text{scy}}\varepsilon^{3}/[(\varepsilon^{3} + 0.41(\varepsilon - \varepsilon_{\text{scy}})^{3} + (\varepsilon - \varepsilon_{\text{scy}})^{2}\varepsilon_{\text{scy}}] \quad (\varepsilon_{\text{scy}} < \varepsilon \leq 2.6\varepsilon_{\text{scy}})$$

$$\sigma = f_{\text{scy}}(-0.01441\varepsilon/\varepsilon_{\text{scy}} + 0.84289) \quad (\varepsilon > 2.6\varepsilon_{\text{scy}}),$$
(17)

$$f_{\rm scv} = \eta (1.212 + B\theta + C\theta^2) f_{\rm ck},$$
 (18)

$$\varepsilon_{\text{scy}} = \varphi[1300 + 14.93f_{\text{cc}} + 1380 + 36(f_{\text{cc}} - 15)]\theta^{0.99}, (19)$$

$$\begin{cases} \sigma = 2f_{\text{scy}} \varepsilon / \varepsilon_{\text{scy}} & (\varepsilon \le 0.4\varepsilon_{\text{scy}}) \\ \sigma = f_{\text{scy}} [-0.55(\varepsilon - \varepsilon_{\text{scy}})^2 + \varepsilon_{\text{scy}}^2] / \varepsilon_{\text{scy}}^2 & (0.4\varepsilon_{\text{scy}} < \varepsilon \\ \le \varepsilon_{\text{scy}}) \\ \sigma = f_{\text{scy}} [0.1328\varepsilon^3 - 0.6312\varepsilon^2 \varepsilon_{\text{scy}} + 0.81\varepsilon\varepsilon_{\text{scy}}^2 + 0.69\varepsilon_{\text{scy}}^3], \end{cases}$$

$$(20)$$

$$/\varepsilon_{\text{scy}}^3 \quad (\varepsilon_{\text{scy}} < \varepsilon \le 2.2\varepsilon_{\text{scy}})$$

$$\sigma = 0.83f_{\text{scy}} \quad (\varepsilon > 2.2\varepsilon_{\text{scy}})$$

$$f_{\text{scv}} = \eta (1.212 + B\theta + C\theta^2) f_{\text{ck}},$$
 (21)

$$\varepsilon_{\text{scy}} = \varphi[1300 + 14.93f_{\text{cc}} + 1,400 + 40(f_{\text{cc}} - 20)]\theta^{0.99},$$
 (22)

where the correction factors η and φ are the cubic polynomials of the calculated strength index $f_{\rm scy}$ and the calculated strain index $\varepsilon_{\rm scy}$ respectively, with respect to the slurry-wrapping recycled aggregate replacement ratio r. The expressions for η and φ are given in the following equations:

for square specimens:

$$\eta = 0.93338 - 0.06031r - 0.02588r^2 + 0.12273r^3$$
, (23)

$$\varphi = 2.2805 - 0.18574r + 2.28096r^2 - 0.62518r^3$$
. (24)

for circular specimens:

$$\eta = 1.07284 + 0.08472r - 0.27195r^2 + 0.19982r^3$$
, (25)

$$\varphi = 3.95915 + 1.8728r - 4.36406r^2 + 4.12331r^3$$
. (26)

Figure 13 compares the calculated stress–strain curve with the test-measured curve for some specimens. The results show a good agreement between the calculated and test-measured curves, indicating the predictability of the whole-process stress–strain curve of the SRACFST using the proposed mathematical expressions.

6 Conclusions

This study presents the results of 20 CFST short columns with varying slurry-wrapping recycled aggregate replacement ratios. The study compares the current calculation codes and analyzes the whole-process stress–strain curves of the specimens, leading to the following conclusions:

 The ultimate strength decreases and then increases as the replacement ratio increases. The strength of SRACFST columns exhibited a minimum at 25% aggregate replacement and a maximum at 100% aggregate replacement. The positive effect of the slurry-wrapping treatment in enhancing matrix porosity outweighs the negative effect

- of the complex ITZ of the recycled aggregate, resulting in a favorable strength performance of the SRACFST columns.
- Circular CFST columns exhibit higher ultimate strength and displacement compared to the square CFST columns at the same slurry-wrapping recycled aggregate replacement ratio.
- 3) The residual bearing ratio of specimens positively correlates with the hoop factor. However, the change in strength improvement factor for circular and square specimens is not significant as the substitution ratios increase.
- 4) Among the codes studied, the European Code EC4 demonstrates more prediction of the ultimate load of specimens and the Chinese Code GB50936 exhibits more calculation stability. In contrast, the American Code AISC360-10 and the Japanese Code AIJ tend to calculate more conservatively.
- 5) The expression for the whole-process stress–strain curve has been established, and the calculated curve shows good agreement with the test-measured curve.
- 6) Slurry-wrapping treatment becomes more complicated for aggregates with particle sizes between 5 and 10 mm. Apply slurry-wrapping treatment to aggregates above 10 mm, which facilitates industrial production.

Acknowledgments: The authors are very grateful to the people involved for their dedication to this work.

Funding information: The project was supported by National Natural Science Foundation of China (No. 51968060), which was gratefully acknowledged.

Author contributions: All authors have accepted responsibility for the entire content of this manuscript and approved its submission.

Conflict of interest: The authors state no conflict of interest.

References

- [1] Xu, Z., Z. Huang, C. Liu, X. Deng, D. Hui, and S. Deng. Research progress on mechanical properties of geopolymer recycled aggregate concrete. *Reviews on Advanced Materials Science*, Vol. 60, No. 1, 2021, pp. 158–172.
- [2] Zhu, P., Y. Hao, H. Liu, X. Wang, and L. Gu. Durability evaluation of recycled aggregate concrete in a complex environment. *Journal of Cleaner Production*, Vol. 273, 2020, id. 122569.
- Fareed, S. and A. U. R. Khan. Strengthening of recycled concrete aggregates two-way RC slabs by externally bonded CFRP.

- International Conference on Fibre-Reinforced Polymer (FRP) Composites in Civil Engineering, 2022.
- [4] Piccinali, A., A. Diotti, G. Plizzari, and S. Sorlini. Impact of recycled aggregate on the mechanical and environmental properties of concrete: a review. *Materials*, Vol. 15, No. 5, 2022, id. 1818.
- [5] Tam, V. W. Y., M. Soomro, and A. C. J. Evangelista. A review of recycled aggregate in concrete applications (2000-2017). Construction and Building Materials, Vol. 172, 2018, pp. 272–292.
- [6] Poon, C. S., Z. H. Shui, and L. Lam. Effect of microstructure of ITZ on compressive strength of concrete prepared with recycled aggregates. *Construction and Building Materials*, Vol. 18, No. 6, 2004, pp. 461–468.
- [7] Shi, C., Y. Li, J. Zhang, W. Li, L. Chong, and Z. Xie. Performance enhancement of recycled concrete aggregate - A review. *Journal of Cleaner Production*, Vol. 112, 2016, pp. 466–472.
- [8] Luo, S., S. Ye, J. Xiao, J. Zheng, and Y. Zhu. Carbonated recycled coarse aggregate and uniaxial compressive stress-strain relation of recycled aggregate concrete. *Construction and Building Materials*, Vol. 188, 2018, pp. 956–965.
- [9] Heidari, A. and D. Tavakoli. A study of the mechanical properties of ground ceramic powder concrete incorporating nano-SiO₂ particles. Construction and Building Materials, Vol. 38, 2013, pp. 255–264.
- [10] Martirena, F., T. Castaño, A. Alujas, R. Orozco-Morales, L. Martinez, and S. Linsel. Improving quality of coarse recycled aggregates through cement coating. *Journal of Sustainable Cement-Based Materials*, Vol. 6, No. 1, 2017, pp. 69–84.
- [11] Zhan, B. J., D. X. Xuan, and C. S. Poon. Enhancement of recycled aggregate properties by accelerated CO₂ curing coupled with limewater soaking process. *Cement & Concrete Composites*, Vol. 89, 2018, pp. 230–237.
- [12] Wang, Y. S., J. L. Zheng, and F. You. Review on enhancement methods of recycled aggregate. *Materials Reports*, Vol. 35, No. 05, 2021, pp. 5053–5061. in Chinese.
- [13] Wang, J., J. Zhang, D. Cao, H. Dang, and B. Ding. Comparison of recycled aggregate treatment methods on the performance for recycled concrete. *Construction and Building Materials*, Vol. 234, 2020, id. 117366.
- [14] Wang, X. G., M. L. Jiang, X. Chen, Y. G. Wang, J. P. Zhu, and F. Cheng. Effect of different pre-soaked aggregate-PVA fiber on the mechanical properties of recycled aggregate concrete. *Acta Materiae Compositae Sinica*, Vol. 39, No. 03, 2022, pp. 1205–1214. in Chinese.
- [15] Shi, C. J., Z. M. Wu, Z. J. Cao, C. L. Tung, and J. L. Zheng. Performance of mortar prepared with recycled concrete aggregate enhanced by CO₂ and pozzolan slurry. *Cement & Concrete Composites*, Vol. 86, 2018, pp. 130–138.
- [16] Hasan, H. G., T. Ekmekyapar, and B. A. Shehab. Mechanical performances of stiffened and reinforced concrete-filled steel tubes under axial compression. *Marine Structures*, Vol. 65, 2019, pp. 417–432.
- [17] Hasan, H. G. and T. Ekmekyapar. Bond-slip behaviour of concrete filled double skin steel tubular (CFDST) columns. *Marine Structures*, Vol. 79, 2021, id. 103061.
- [18] Ekmekyapar, T. and H. G. Hasan. The influence of the inner steel tube on the compression behaviour of the concrete filled double skin steel tube (CFDST) columns. *Marine Structures*, Vol. 66, 2019, pp. 197–212.
- [19] Tam, V. W. Y., Z. Tao, and A. Evangelista. Performance of recycled aggregate concrete filled steel tubular (RACFST) stub columns with expansive agent. *Construction and Building Materials*, Vol. 272, 2021, id. 121627.

- [20] Xiao, J. Z., J. Yang, H. J. Huang, and Z. P. Wang. Experimental study on recycled concrete confined by steel tube under axial compression. *Journal of Building Structures*, Vol. 32, No. 6, 2011, pp. 92–98. in Chinese.
- [21] Ke, X., W. Xiang, X. Peng, and Y. Dan. Axial compression performance and residual strength calculation of concrete-encased CFST composite columns exposure to high temperature. *Applied Sciences-Basel*, Vol. 12, No. 1, 2022, id. 480.
- [22] Zhang, X., X. Gao, Y. Ding, P. Xu, G. Zhou, and J. Xu. Axial compression behavior of basalt fiber-reinforced recycled aggregate concrete-filled square steel tubular stub column. *Structural Concrete*, Vol. 23, No. 1, 2022, pp. 365–381.
- [23] Lyu, W. Q., L. H. Han, and C. Hou. Axial compressive behaviour and design calculations on recycled aggregate concrete-filled steel tubular (RAC-FST) stub columns. *Engineering Structures*, Vol. 241, 2021, id. 112452.
- [24] Zhou, C., W. Chen, X. Ruan, and X. Tang. Experimental study on axial compression behavior and bearing capacity analysis of high titanium slag CFST columns. *Applied Sciences-Basel*, Vol. 9, No. 10, 2019, id. 2021.
- [25] Bahrami, A. and M. Nematzadeh. Bond behavior of lightweight concrete-filled steel tubes containing rock wool waste after exposure to high temperatures. *Construction and Building Materials*, Vol. 300, 2021, id. 124039.
- [26] Karimi, A., M. Nematzadeh, and S. Mohammad-Ebrahimzadeh-Sepasgozar. Analytical post-heating behavior of concrete-filled steel tubular columns containing tire rubber. *Computers & Concrete*, Vol. 6, 2020, id. 26.
- [27] Liang, J., S. Lin, and M. Ahmed. Axial behavior of carbon fiberreinforced polymer–confined recycled aggregate concrete-filled steel tube slender square columns. *Advances in Structural Engineering*, Vol. 24, No. 15, 2021, pp. 3507–3518.
- [28] Liang, J., S. Lin, W. Li, and D. Liu. Axial compressive behavior of recycled aggregate concrete-filled square steel tube stub columns strengthened by CFRP. *Structures*, Vol. 29, 2021, pp. 1874–1881.
- [29] Lin, S., Y.-G. Zhao, J. Li, and Z. H. Lu. Confining stress path-based compressive strength model of axially loaded FRP-confined columns. *Journal of Composites for Construction*, Vol. 25, No. 1, 2021, id. 04020077.
- [30] de Azevedo, V. S., L. R. O. de Lima, P. C. G. S. Vellasco, M. Tavares, and T. M. Chan. Experimental investigation on recycled aggregate concrete filled steel tubular stub columns under axial compression. *Journal of Constructional Steel Research*, Vol. 187, 2021, id. 106930.
- [31] JGJ 52-2006. Standard for technical requirements and test method of sand and crushed stone (or gravel) for ordinary concrete. *China Academy of Building Research*, 2006.
- [32] GB/T 228.1-2010. Metallic materials-tensile testing-part 1: method of test at room temperature. *China National Standardization Administration Committee*, 2010.
- [33] G.T. 50081-2019. Standard for test methods of concrete physical and mechanical properties. China Architecture & Building Press, 2019.
- [34] Gao, S., Z. Peng, L. Guo, F. Fu, and Y. Wang. Compressive behavior of circular concrete-filled steel tubular columns under freeze-thaw cycles. *Journal of Constructional Steel Research*, Vol. 166, 2020, id. 105934.
- [35] Chen, Z. P., X. J. Ke, J. Y. Xue, and Y. S. Su. Mechanical performance and ultimate bearing capacity calculation of steel tube confined recycled coarse aggregate concrete. *China Civil Engineering Journal*, Vol. 46, No. 2, 2013, pp. 70–77. in Chinese.

- [36] Wang, Y. Y., J. Chen, and Y. Geng. Testing and analysis of axially loaded normal-strength recycled aggregate concrete filled steel tubular stub columns. *Engineering Structures*, Vol. 86, 2015, pp. 192–212.
- [37] Li, P., Y. Zhou, T. Yang, Q. Yang, and F. Xing. Axial compressive behavior of seawater sea-sand recycled aggregate concrete-filled double-skin non-corrosive tubular columns with square cross-section. *Thin-Walled Structures*. Vol. 167, 2021, id. 108213.
- [38] Wang, J. H., C. L. Zheng, B. H. Jin, Y. D. Zhao, S. X. Li, X. Z. Li, et al. Effect of fly ash/different aggregates on the mechanical properties of fibre reinforced self-compacting recycled concrete. *Journal of Functional Materials*, Vol. 53, No. 9, 2022, pp. 9209–9218. in Chinese.
- [39] Mehta, P. K. and P. Monteiro. Concrete: microstructure, properties, and materials, Concrete: microstructure, properties, and materials. 2013.
- [40] Chen, Z. P., D. H. Zhan, and J. J. Xu. Research on mechanical properties of recycled concrete using different recycled coarse aggregate replacement. *Industrial Construction*, Vol. 45, No. 1, 2015, pp. 130–135. in Chinese.
- [41] Chen, J., S. Zhang, Y. Wang, and Y. Geng. Axial compressive behavior of recycled concrete filled steel tubular stub columns with the inclusion of crushed brick. *Structures*, Vol. 26, 2020, pp. 271–283.
- [42] Wang, Y. Y., J. Chen, B. Zong, and Y. Geng. Mechanical behavior of axially loaded recycled aggregate concrete filled steel tubular stubs and reinforced recycled aggregate concrete stubs. *Journal of Building Structures*, Vol. 32, No. 12, 2011, pp. 170–177. in Chinese.
- [43] Xiao, J. Z. Experimental investigation on complete stress-strain curve of recycled concrete under uniaxial loading. *Journal of Tongji University(Natural Science)*, Vol. 11, 2007, pp. 1445–1449.
- [44] Cai, J. M., J. L. Pan, and Q. F. Shan. Failure mechanism of full-size concrete filled steel circle and square tubes under uniaxial compression. *Science China-Technological Sciences*, Vol. 58, No. 10, 2015, pp. 1638–1647.
- [45] Lam, L. and J. G. Teng. Design-oriented stress-strain model for FRP-confined concrete in rectangular columns. *Journal of Reinforced Plastics and Composites*, Vol. 22, No. 13, 2003, pp. 1149–1186.
- [46] Yan, J. B., Z. Wang, and J. Xie. Compressive behaviours of double skin composite walls at low temperatures relevant to the

- arctic environment. *Thin-Walled Structures*, Vol. 140, 2019, pp. 294–303.
- [47] Yan, J. B., Y. L. Luo, X. C. Lin, Y. B. Luo, N. X. Zhang, and Q. F. Liu. Studies on axial compressive behavior of square concrete filledhigh-strength steel tube columns in cold regions, *Journal of Tianjin University(Science and Technology)*. Vol. 55, No. 4, 2022, pp. 402–410. in Chinese.
- [48] Wang, Y. B., C. Song, X. Y. Zhao, and G. Li. Experimental study on behavior of circular concrete-filled high-strength steel tubular stub columns under compression. *Journal of Building Structures*, Vol. 43, No. 11, 2022, pp. 221–234. in Chinese.
- [49] Han, L. H. *Concrete filled steel tubular structures—theory and practice*, 3rd edn, Beijing: China Science Press: 2016.
- [50] Shen, M., W. Huang, J. Liu, and Z. Zhou. Axial compressive behavior of rubberized concrete-filled steel tube short columns. *Case Studies in Construction Materials*, Vol. 16, 2022, id. e00851.
- [51] Li, P., J. Hu, F. Xing, L. Sui, Y. Zhou, and C. Chen. Behavior and modeling of double-skin tubular columns filled by ultra-lightweight cement composites (ULCCs). *Composite Structures*, Vol. 263, 2021, id. 113709.
- [52] GB50936. Technical code for concrete filled steel tubular structures, Ministry of Construction of the People's Republic of China. 2014.
- [53] Eurocode 4. Design of composite steel and concrete structures. part 1-1: general rules and rules for building, European Committee for Standardization, 2004.
- [54] AISC360-10. Specification for structural steel buildings, American Institute of Steel Construction, 2010.
- [55] AIJ. Recommendations for design and construction of concrete filled steel tubular structures, Architectural Institute of Japan, 2008.
- [56] Eurocode 2. Design of concrete structures general rules and rules for buildings, British Standards Institution, 2004.
- [57] GB50010-2010. Code for design of concrete structures, China Academy of Building Research, 2010.
- [58] X. G. Zhang, G. Q. Zhou, Y. H. Fan, X. Gao, F. G. Leng, and F. Wang. Axial compressive property of circular steel tubular stub column filled with basalt-fiber reinforced recycled-concrete. *Acta Materiae Compositae Sinica*, Vol. 40, No. 1, 2023, pp. 369–382 in Chinese.